

# Stein Variational Gaussian Processes

Thomas Pinder<sup>1</sup>, Christopher Nemeth<sup>1</sup>, David Leslie<sup>1</sup>

<sup>1</sup>Department of Mathematics and Statistics, Lancaster University, UK

January 20, 2022

## Abstract

We show how to use Stein variational gradient descent (SVGD) to carry out inference in Gaussian process (GP) models with non-Gaussian likelihoods and large data volumes. Markov chain Monte Carlo (MCMC) is extremely computationally intensive for these situations, but the parametric assumptions required for efficient variational inference (VI) result in incorrect inference when they encounter the multimodal posterior distributions that are common for such models. SVGD provides a non-parametric alternative to variational inference which is substantially faster than MCMC. We prove that for GP models with Lipschitz gradients the SVGD algorithm monotonically decreases the Kullback-Leibler divergence from the sampling distribution to the true posterior. Our method is demonstrated on benchmark problems in both regression and classification, a multimodal posterior, and an air quality example with 550,134 spatiotemporal observations, showing substantial performance improvements over MCMC and VI.

## 1 Introduction

Gaussian processes (GPs) are highly expressive, non-parametric distributions over continuous functions and are frequently employed in both regression and classification tasks (Rasmussen and Williams, 2006). In recent years, GPs have received significant attention in the machine learning community due to their successes in domains such as reinforcement learning (Deisenroth et al., 2015), variance reduction (Oates et al., 2017), and optimisation (Mockus, 2012). This recent blossoming has been facilitated by advances in inference methods, and especially by variational inference (VI) which provides a tractable approach to fitting GP models to large and/or non-Gaussian data sets (e.g. Hensman et al., 2013; Cheng and Boots, 2017).

While computationally efficient, VI typically relies on the practitioner placing a parametric constraint upon the approximating posterior distribution. Unfortunately, this assumption can often severely inhibit the quality of the approximate posterior should the true posterior not belong to the chosen family of probability distributions, as often happens with GPs (Havasi et al., 2018). The most common (asymptotically) exact inference method for GPs is Markov chain Monte-Carlo (MCMC). However, sampling can be problematic if the posterior distribution is non-convex as the sampler can become trapped in local modes (Rudoy and Wolfe, 2006). Additionally, MCMC does not enjoy the same computational scalability as VI, and for this reason it is impractical for modelling problems with a large number of observations.

In this work we propose the use of Stein Variational Gradient Descent (SVGD) (Liu and Wang, 2016), a non-parametric VI approach, as an effective inference method for GP models. SVGD can be thought of as a particle-based approach, whereby particles

Table 1: Features of key inference methods for GP models.

Reference	$p(\mathbf{y} \mathbf{f})$	Sparse	Approx. posterior	Hyperparams	Inference
Opper and Archambeau (2008)	Binary	✗	Gaussian	Point estimate	Variational
Titsias (2009)	Gaussian	✓	Gaussian	Point estimate	Variational
Nguyen and Bonilla (2014)	Any	✗	Gaussian mixture	Point estimate	Variational
Hensman et al. (2015)	Any	✓	True posterior	Marginalised	MCMC
This work	Any	✓	True posterior	Marginalised	SVGD

are sequentially transformed until they become samples from an arbitrary variational distribution that closely approximates the posterior of interest. SVGD can be considered a hybrid of VI and Monte Carlo approaches, yielding benefits over both. The first benefit is removing the parametric assumption used in VI. The result of this is that inference through SVGD allows a richer variational distribution to be learned. A second benefit is that we do not need to compute the acceptance step required in MCMC. This leads to greater efficiency in SVGD as we are only required to compute the score function, an operation that can be accelerated for big datasets using the subsampling trick in Section 4. Finally, through the use of a kernel function acting over the set of particles, SVGD encourages full exploration over the posterior space, meaning that we are able to better represent the uncertainty in multimodal posteriors. This is a critical difference in the quality of inference that is possible through SVGD in comparison to alternative methods and we provide compelling empirical evidence to support this in Section 5.2. Table 1 shows the position of this work within the current literature.

Our article demonstrates how to use SVGD to fit GPs to both Gaussian and non-Gaussian data, including when computational scalability is addressed through an inducing point representation of the original data. We prove that the SVGD scheme reduces the Kullback-Leibler (KL) divergence to the target distribution on each iteration. We empirically demonstrate the performance of SVGD in a range of both classification and regression datasets, comparing against traditional VI and modern implementations of MCMC for GPs, including in a large-scale spatiotemporal model for air quality in the UK. We release, at <https://github.com/RedactedForReview>, code for reproducing the experiments in Section 5, and a general library for fitting GPs using SVGD based entirely upon GPFlow (Matthews et al., 2017) and TensorFlow (Abadi et al., 2016). For a demonstration of package see Appendix 11.

## 2 Stein Variational Gradient Descent

**Stein’s discrepancy** The foundation for SVGD is Stein’s identity (Stein, 1972). For an arbitrary (continuously differentiable) density of interest  $p$ ,

$$\mathbb{E}_{\boldsymbol{\lambda} \sim p} \left[ \underbrace{\phi(\boldsymbol{\lambda}) \nabla_{\boldsymbol{\lambda}} \log p(\boldsymbol{\lambda}) + \nabla_{\boldsymbol{\lambda}} \phi(\boldsymbol{\lambda})}_{\text{Stein operator: } \mathcal{A}_p \phi(\boldsymbol{\lambda})} \right] = 0, \quad (1)$$

where  $\phi$  belongs to a family of smooth functions  $\mathcal{F}$ . Stein’s identity has found uses in a range of modern machine learning problems including variance reduction (Oates et al., 2017), model selection (Kanagawa et al., 2019) and generative modelling (Pu et al., 2017). In our application,  $p$  will be the posterior density of interest. We can identify the internals of the expectation in (1) as the *Stein operator*, a quantity we denote as  $\mathcal{A}_p \phi(\boldsymbol{\lambda})$ .

Stein’s identity (1) can be used to give a notion of *distance* between any two probability distributions. Replacing the density  $p$  under which we evaluate the expectation in (1) with a second density  $q$ , (1) is 0 if and only if  $p = q$ . For a class of functions  $\mathcal{F}$ , the Stein discrepancy is defined to be

$$\sqrt{\mathbb{D}(q, p)} = \sup_{\phi \in \mathcal{F}} \mathbb{E}_{\boldsymbol{\lambda} \sim q} [\text{trace}(\mathcal{A}_p \phi(\boldsymbol{\lambda}))]. \quad (2)$$

Note that when  $\phi$  is  $d \times 1$  vector-valued function, the expectation term in (1) yields a  $d \times d$  matrix so the trace operator is applied (i.e.,  $\mathbb{E}[\text{trace}(\mathcal{A}_p \phi(\boldsymbol{\lambda}))]$ ) to conserve the computation of a scalar value.

Taking  $\mathcal{F}$  to be the unit ball of the Reproducing Kernel Hilbert Space (RKHS)  $\mathcal{H}^d$  of a positive definite kernel  $\kappa(x, x')$ , we can optimise (2) explicitly (Liu et al., 2016). This functional optimisation yields the following closed form solution to (2)

$$\hat{\phi}(\boldsymbol{\lambda}) = \beta(\boldsymbol{\lambda}) / \|\beta\|_{\mathcal{H}^d} \quad \text{where } \beta(\boldsymbol{\lambda}) = \mathbb{E}_{\boldsymbol{\lambda}' \sim q} [\mathcal{A}_p \kappa(\boldsymbol{\lambda}, \boldsymbol{\lambda}')]. \quad (3)$$

**Stein Variational Gradient Descent** In SVGD, as in classical VI, we approximate the true posterior distribution  $p$  with a variational distribution  $q$  that minimises the KL divergence between  $p$  and  $q$ . The innovation in SVGD is that we assume no parametric form for  $q$ . From an arbitrary initial distribution  $q_0$ , SVGD iterates through a series of pushforward transformations that reduce the KL divergence between the target distribution and the distribution  $q_t$  after  $t$  iterations.

In particular, the transformation is defined by considering a mapping  $\mathcal{T}(\boldsymbol{\lambda}) = \boldsymbol{\lambda} + \epsilon \phi(\boldsymbol{\lambda})$  for an arbitrary function  $\phi$  and perturbation magnitude  $\epsilon$ , where  $\boldsymbol{\lambda} \sim q_t$ . The transformed distribution  $q_{t+1}$  is the distribution of  $\mathcal{T}(\boldsymbol{\lambda})$ . Following Gorham and Mackey (2015) and Liu et al. (2016), we assume  $\phi$  lives in the RKHS  $\mathcal{H}^d$ . Under this assumption, it can be shown that

$$\nabla_{\epsilon} \text{KL}(q_{t+1} \| p)|_{\epsilon=0} = -\mathbb{E}_{\boldsymbol{\lambda} \sim q_t} [\text{trace}(\mathcal{A}_p \phi(\boldsymbol{\lambda}))]. \quad (4)$$

Comparing (4) and (2) we see that using  $\phi = \hat{\phi}$  from (3) maximally decreases the KL divergence.

To implement the recursion, we maintain a finite set of  $J$  samples that empirically represent  $q$ , referred to as *particles*. These particles  $\Lambda = \{\boldsymbol{\lambda}^j\}_{j=1}^J$  are initially sampled independently from  $q_0$ , which is typically taken to be the prior distribution.<sup>1</sup> The transformation  $\mathcal{T}$  is then applied repeatedly to the set of particles, where at each stage the optimal  $\phi$  from (3) is estimated empirically using the particles  $\Lambda_t = \{\boldsymbol{\lambda}_t^m\}_{m=1}^J$  at the  $t^{\text{th}}$  iteration:

$$\hat{\phi}_{\Lambda_t}(\boldsymbol{\lambda}) = \frac{1}{J} \sum_{j=1}^J \left[ \underbrace{\kappa(\boldsymbol{\lambda}_t^j, \boldsymbol{\lambda}) \nabla_{\boldsymbol{\lambda}} \log p(\boldsymbol{\lambda}_t^j)}_{\text{Attraction}} + \underbrace{\nabla_{\boldsymbol{\lambda}} \kappa(\boldsymbol{\lambda}_t^j, \boldsymbol{\lambda})}_{\text{Repulsion}} \right]. \quad (5)$$

When the process terminates after  $T$  iterations, each of the particles is a sample from a distribution  $q_T$  with low KL divergence from the target  $p$ , and we can use the particles in the same way as a standard Monte Carlo sample.

Examining the update step in (5), it can be seen that the first term transports particles towards areas in the posterior distribution that represent high probability mass. Conversely, the second term is the derivative of the kernel function; a term that will penalise particles

<sup>1</sup>In the asymptotic limit, the final particle values are invariant to the initial distribution that particles are initialised from (Papamakarios et al., 2019)

being too close to one another (see Appendix 7). In the case that  $J = 1$ , the summation in (5) disappears, and the entire scheme reduces to regular gradient based optimisation. Additionally, there is no danger of running SVGD with  $J$  too large as, by the *propagation of chaos* (Kac, 1976), the final distribution of the  $i^{\text{th}}$  particle is invariant to  $J$  as the number of iteration steps  $T \rightarrow \infty$  (Liu and Wang, 2016).

**Connection to variational inference** Typically, in VI we minimise the KL divergence between a  $\xi$ -parameterised variational distribution  $q_\xi(\boldsymbol{\lambda})$  and the target density:

$$\xi^* = \arg \min_{\xi} \text{KL}(q_\xi(\boldsymbol{\lambda}) || p(\boldsymbol{\lambda})). \quad (6)$$

$\xi$  often parameterises a family  $\{q_\xi\}$  of Gaussian distributions. The resultant parameters  $\xi^*$  are then used to form the optimal variational distribution  $q_{\xi^*}(\boldsymbol{\lambda})$ , used in place of the intractable  $p(\boldsymbol{\lambda})$ .

In a regular VI framework, the explicit form placed on  $q$  can be highly restrictive, particularly if the true posterior density is not well approximated by the variational family selected. The nonparametric approach of SVGD allows for a more flexible representation of the posterior geometry beyond the commonly used Gaussian distribution used in regular VI. An additional advantage is that SVGD only requires evaluation of the posterior’s score function, a quantity that is invariant to the normalisation constant and can be unbiasedly approximated in large data settings.

**Related SVGD work** SVGD has been used in the context of fitting Bayesian logistic regression and Bayesian neural networks (Liu, 2017). Further, SVGD was used in the context of variational autoencoders (VAE) to model the latent space (Pu et al., 2017). By relaxing the Gaussian assumption that is typically made of the latent space, it was possible to learn a more complex distribution over the latent space of the VAE. Further examples of the applications of SVGD can be found in reinforcement learning (Liu, 2017), Bayesian optimisation (Gong et al., 2019), and in conjunction with deep learning (Grathwohl et al., 2020). Theoretical analysis has also established connections between SVGD and the overdamped Langevin diffusion (Duncan et al., 2019), and black-box variational inference (Chu et al., 2020).

This article leverages the effective and efficient SVGD optimisation framework to address the computational and multi-modality challenges endemic in GP inference. We show that compared to standard inference approaches for GPs, the SVGD framework offers the best trade-off between accuracy, computational efficiency and model flexibility.

### 3 Gaussian Processes

Consider data  $(X, \mathbf{f}, \mathbf{y}) = \{\mathbf{x}_i, f_i, y_i\}_{i=1}^N$  where  $x_i \in \mathbb{R}^d$ , and  $y_i \in \mathbb{R}$  is a stochastic observation depending on  $f_i = f(x_i)$  for some latent function  $f$ . Let  $k_\theta(\mathbf{x}, \mathbf{x}')$  be a positive definite kernel function parameterised by a set of hyperparameters  $\boldsymbol{\theta}$  with resultant Gram matrix  $K_{\mathbf{xx}} = k_\theta(\mathbf{x}, \mathbf{x}')$ . Following standard practice in the literature and assuming a zero mean function, we can posit the hierarchical GP framework as

$$\begin{aligned} p(\mathbf{y} | \mathbf{f}, \boldsymbol{\theta}) &= \prod_{i=1}^N p(y_i | f_i, \boldsymbol{\theta}), \\ \mathbf{f} | X, \boldsymbol{\theta} &\sim \mathcal{N}(0, K_{\mathbf{xx}}), \\ \boldsymbol{\theta} &\sim p_0. \end{aligned} \quad (7)$$

---

**Algorithm 1** Pseudocode for fitting a Gaussian process using  $T$  iterations of SVGD.

---

**Require:** Base distribution  $q_0$ . Target distribution  $p(\boldsymbol{\lambda} | X, \mathbf{y})$  where  $\boldsymbol{\lambda} = \{\boldsymbol{\theta}, \boldsymbol{\nu}\}$ .  
 Create  $\Lambda_0 = \{\boldsymbol{\lambda}_0^j\}_{j=1}^J$  where  $\boldsymbol{\lambda}_0^j \stackrel{\text{iid}}{\sim} q_0$ .  
**for**  $t$  in  $1:T$  **do**  
   **for**  $j$  in  $1:J$  **do**  
      $\boldsymbol{\lambda}_t^j \leftarrow \boldsymbol{\lambda}_{t-1}^j + \epsilon \hat{\phi}_{\Lambda_{t-1}}(\boldsymbol{\lambda}_{t-1}^j)$  (see (5))  
   **end for**  
    $\Lambda_t = \{\boldsymbol{\lambda}_t^j\}_{j=1}^J$   
**end for**  
**return**  $\Lambda_T$

---



---

**Algorithm 2** Pseudocode for predictive inference over test inputs  $X^*$ .

---

**Require:** Learned set of particles  $\{\boldsymbol{\lambda}_j\}_{j=1}^J$   
 Initialise **sample** =  $\{\}$   
**for**  $j$  in  $1:J$  **do**  
   Set  $(\boldsymbol{\theta}, \boldsymbol{\nu}) = \boldsymbol{\lambda}^j$   
   **for**  $k$  in  $1:K$  **do**  
     Sample  $\mathbf{y}^* \sim p(\cdot | X^*, \boldsymbol{\theta}, \boldsymbol{\nu})$   
     Append  $\mathbf{y}^*$  to **sample**  
   **end for**  
**end for**  
**return**  $\text{mean}(\text{sample}), \text{var}(\text{sample})$

---

From the generative model in (7), we can see that the posterior distribution of a GP is

$$p(\mathbf{f}, \boldsymbol{\theta} | \mathbf{y}) = \frac{1}{C} p(\mathbf{y} | \mathbf{f}, \boldsymbol{\theta}) p(\mathbf{f} | \boldsymbol{\theta}) p_0(\boldsymbol{\theta}), \quad (8)$$

where  $C$  denotes the unknown normalisation constant of the posterior. Often we are interested in using the posterior to make new function predictions  $f^*$  for test data  $X^*$ ,

$$p(\mathbf{f}^* | \mathbf{y}) = \iint p(\mathbf{f}^* | \mathbf{f}, \boldsymbol{\theta}) p(\mathbf{f}, \boldsymbol{\theta} | \mathbf{y}) d\boldsymbol{\theta} d\mathbf{f}. \quad (9)$$

When the likelihood  $p(y_i | f_i, \boldsymbol{\theta})$  is Gaussian, the posterior predictive distribution conditional on  $\boldsymbol{\theta}$  is analytically available as we can marginalise  $\mathbf{f}$  out from (9), and inference methods focus on  $\boldsymbol{\theta}$ . For non-Gaussian likelihoods, we must approximate the integral over  $\mathbf{y}$  using alternative approaches. Some of the most common methods are Laplace approximations (Williams and Barber, 1998), expectation-propagation (Minka, 2001; Hernández-Lobato and Hernández-Lobato, 2016), MCMC (Murray et al., 2010), or VI (Opper and Archambeau, 2008).

Even when  $\mathbf{f}$  can be marginalised, computing (9) requires the inversion of  $K_{\mathbf{xx}}$ , an operation that requires  $\mathcal{O}(N^3)$  computation. To reduce this cost when  $N$  is large, one can introduce a set of *inducing points*  $Z = \{\mathbf{z}_i\}_{i=1}^M$  that live in the same space as  $X$ , such that  $M \ll N$  (Snelson and Ghahramani, 2005). The fundamental assumption made in the majority of sparse frameworks (see Quiñero-Candela and Rasmussen, 2005) is that the elements of  $\mathbf{f}$  and  $\mathbf{f}^*$  are conditionally independent given  $\mathbf{u} = f(Z)$ . Inference within this model only requires inversion of the Gram matrix  $K_{\mathbf{ZZ}} = k_{\boldsymbol{\theta}}(Z, Z)$ , which reduces the cost for posterior inference from  $\mathcal{O}(N^3)$  to  $\mathcal{O}(NM^2)$ .

Inference for sparse GP models has thus far either required the GP hyperparameters  $\boldsymbol{\theta}$  to be fixed so that VI can be deployed (e.g. Titsias, 2009; Hensman et al., 2013), or has used extremely computationally-intensive MCMC schemes (e.g. Hensman et al., 2015). A full review of scalable GPs can be found in Liu et al. (2019).

We demonstrate that SVGD is able to retain the ability to carry out joint inference over  $\mathbf{f}$ ,  $\boldsymbol{\theta}$  and, where necessary,  $\mathbf{u}$  without incurring the large overheads of MCMC schemes. In the rest of this article we do not explicitly discuss inference in sparse GPs, but all our results apply equally to sparse formulations as to the full GP models discussed; the sparse approximation simply corresponds to a variant GP (Quiñero-Candela and Rasmussen, 2005).

Table 2: Mean test log-likelihoods (larger is better) over 5 independent data splits, with bold values indicating the best performing method. Our SteinGP with 2, 5, 10 and 20 particles is compared against a GP fitted using VI, maximum likelihood (ML) and Hamiltonian Monte-Carlo (HMC) (Note, HMC is used for classification datasets (listed in blue) as an ML approach is intractable). For brevity, only the datasets where there is a significant difference between the best performing and one, or more, alternative methods are reported here. The full table can be found in Table 8 in Appendix 10.2

Dataset	SteinGP2	SteinGP5	SteinGP10	SteinGP20	VI	ML/HMC
Airfoil	<b>0.06 ± 0.04</b>	0.06 ± 0.04	0.05 ± 0.06	0.05 ± 0.05	0.03 ± 0.03	0.03 ± 0.03
Blood	-0.6 ± 0.05	-0.6 ± 0.04	-0.6 ± 0.05	-0.61 ± 0.04	<b>-0.51 ± 0.05</b>	-0.52 ± 0.06
Breast Cancer	-0.08 ± 0.04	-0.08 ± 0.02	-0.08 ± 0.02	<b>-0.08 ± 0.01</b>	-0.65 ± 0.09	<b>-0.08 ± 0.04</b>
Challenger	-1.53 ± 0.45	-1.52 ± 0.43	<b>-1.46 ± 0.32</b>	-1.53 ± 0.41	-1.51 ± 0.3	-1.51 ± 0.3
Concretelump	1.08 ± 0.39	1.07 ± 0.41	<b>1.06 ± 0.4</b>	1.08 ± 0.39	0.13 ± 1.14	0.13 ± 1.14
Fertility	-0.44 ± 0.03	-0.44 ± 0.03	-0.43 ± 0.02	<b>-0.42 ± 0.02</b>	-0.70 ± 0.08	-0.54 ± 0.02
Gas	0.88 ± 0.11	0.88 ± 0.11	<b>0.89 ± 0.1</b>	0.88 ± 0.11	0.79 ± 0.11	0.79 ± 0.11
Hepatitis	-0.41 ± 0.07	-0.41 ± 0.07	-0.42 ± 0.07	<b>-0.4 ± 0.07</b>	-0.69 ± 0	-0.44 ± 0.04
Parkinsons	4.12 ± 0.05	4.12 ± 0.05	<b>4.14 ± 0.03</b>	4.13 ± 0.06	3.95 ± 0.04	3.95 ± 0.04
Spectf	-0.26 ± 0.01	-0.26 ± 0.01	-0.26 ± 0.01	<b>-0.26 ± 0.01</b>	-0.69 ± 0	-0.68 ± 0.03
Winewhite	0.56 ± 0.05	0.57 ± 0.05	<b>0.57 ± 0.05</b>	0.57 ± 0.05	0.49 ± 0.05	0.55 ± 0.05

## 4 Stein Variational Gaussian Processes

**Gaussian data** Recalling the posterior distribution (8) of a GP, we seek to approximate this distribution using a finite set of particles learned through SVGD. When the data likelihood is Gaussian, we are able to analytically integrate out  $f$  and use SVGD to learn the kernel hyperparameters and observation noise  $\sigma^2$ , which comprise  $\theta$ . This means that each particle  $\lambda^j$  represents a sampled  $\theta$  value. SVGD is useful even in these cases, as estimating kernel parameters such as the lengthscale can be particularly challenging for VI and MCMC. This is due to their unidentifiable nature that often manifests itself through a multimodal marginal posterior distribution (see Section 5.2 for an example of this). Through a set of interacting particles, SVGD is able to efficiently capture these modes. Accounting for posterior mass beyond the dominant mode is of utmost importance when trying to give realistic posterior predictions (Palacios and Steel, 2006; Gelfand et al., 2010).

**Non-Gaussian data** In the general GP setup in (7), where  $y_i | f_i, \theta$  is non-Gaussian, we are required to learn the latent values  $\mathbf{f}$  of the GP in addition to  $\theta$ . To decouple the strong dependency that exists between  $\mathbf{f}$  and  $\theta$ , we centre (or ‘whiten’) the GP’s covariance matrix such that  $\mathbf{f} = L_\theta \boldsymbol{\nu}$ , where  $L_\theta$  is the lower Cholesky decomposition of the Gram matrix  $K_{\mathbf{xx}}$ , and  $\nu_i \sim \mathcal{N}(0, 1)$ . Applying such a transformation has been shown to enhance the performance of inferential schemes in the GP setting (Murray et al., 2010; Hensman et al., 2015; Salimbeni and Deisenroth, 2017). Once whitened, we can use the joint posterior distribution  $p(\theta, \boldsymbol{\nu} | X, \mathbf{y})$  as the target distribution for SVGD and *post hoc* deterministically transform the posterior samples to give  $p(\theta, \mathbf{f} | X, \mathbf{y})$ .

SVGD requires evaluation of the score function of the density at the current particle values to evaluate (5). Using automatic differentiation, this is a trivial task. However, it is accompanied by a computational cost that scales quadratically with  $N$  since we can no longer marginalise  $\mathbf{f}$ . For this reason, in datasets surpassing several thousand datapoints, we estimate the score function using subsampled mini-batches  $\Psi \subset \{1, \dots, N\}$ . The end

result of this is a score function approximation that can be written as

$$\nabla_{\boldsymbol{\theta}, \boldsymbol{\nu}} \log p(\boldsymbol{\theta}, \boldsymbol{\nu} | X, \mathbf{y}) \approx \nabla_{\boldsymbol{\theta}, \boldsymbol{\nu}} \log p_0(\boldsymbol{\theta}, \boldsymbol{\nu}) + \frac{N}{|\Psi|} \sum_{i \in \Psi} \nabla_{\boldsymbol{\theta}, \boldsymbol{\nu}} \log p(\mathbf{y}_i | \boldsymbol{\theta}, \boldsymbol{\nu}_i). \quad (10)$$

**Posterior predictions** Once a set of particles  $\Lambda$  has been learned, we can use the value of each particle to make predictive inference. Recalling that the primary motivation of SVGD is to enable accurate predictive inference in posterior distributions with complex and multimodal geometries, naively taking the mean particle value for each parameter as the final estimate of each parameter in the GP could become problematic when the posterior is complex. For this reason, to obtain a predictive mean and variance, we sample  $K$  times from the predictive posterior of the GP for each of the  $J$  particles and compute the mean and variance of the predictive samples. To elucidate this notion, the procedure is summarised in Algorithm 2 .

**Optimisation guarantees** We would like to show that the SteinGP in Algorithm 1 iteratively improves the posterior approximation. Consider the variational distributions  $q_t$  of the particles at time  $t$ . We can show that the Kullback-Leibler divergence between these distributions and the target  $p$  decreases monotonically as  $t$  increases. The following result is similar to that of Liu (2017) and Korba et al. (2020) but with different assumptions and an alternative proof construction. This serves as a useful starting point for more rigorous analysis of GPs (e.g., (Burt et al., 2020)).

**Theorem 1** *Consider SVGD in a general model with  $\log p(\boldsymbol{\lambda})$  at least twice continuously differentiable and  $\nabla \log p(\boldsymbol{\lambda})$  is smooth with Lipschitz constant  $L$ . The Kullback-Leibler divergence between the target distribution  $p$  and its SVGD approximation  $q_t$  at iteration  $t$  is monotonically decreasing, satisfying*

$$KL(q_{t+1} || p) - KL(q_t || p) \leq -\epsilon \mathbb{D}(q_t, p)^2 (1 - \epsilon \mathbb{E}_{\boldsymbol{\lambda} \sim q_t} [L\kappa(\boldsymbol{\lambda}, \boldsymbol{\lambda})/2 + \nabla_{\boldsymbol{\lambda}, \boldsymbol{\lambda}} \kappa(\boldsymbol{\lambda}, \boldsymbol{\lambda})]) \quad (11)$$

It can be shown that for the GP models considered in this paper, the gradients are Lipschitz smooth and therefore Theorem 1 holds. Additionally, Theorem 8 of Gorham and Mackey (2015) establishes weak convergence for a sequence of probability measures  $(q_t)_{t \geq 1}$ , where  $q_t \implies p$  if  $\mathbb{D}(q_t, p) \rightarrow 0$ , and so it follows from Theorem 1, that  $q_t \implies p$  as  $t \rightarrow \infty$ .

## 5 Experiments

**Benchmark datasets** For the datasets used in Section 5.1, models are fitted using 70% of the full dataset, whilst the remaining 30% is used for model assessment. The partitioning of data, hyperparameter initialisation and computing environment used is the same for all models. For each dataset we standardise the inputs and outputs to zero mean and unit standard deviation.

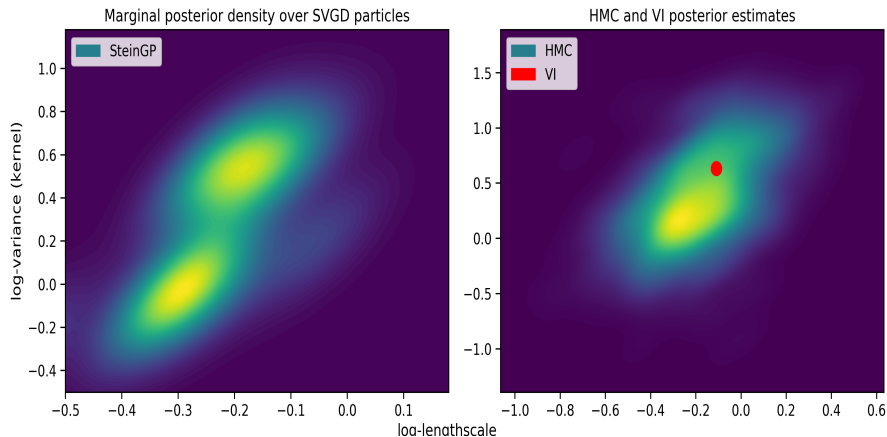


Figure 1: The marginal posterior distributions of the GP model’s kernel parameters in the multimodal example of Section 5.2. The left panel shows the bimodal posterior learned through SVGD, whereas the HMC inferred posterior appears to have just explored a single mode. In order to obtain a tractable evidence lower bound (ELBO) objective for the VI optimiser, model hyperparameters are treated as variational parameters (Titsias, 2009). Consequently, only scalar values for the hyperparameters can be learned. This scalar pair is depicted by the red point in the right panel.

**SVGD implementation details** Throughout our experiments we use an RBF kernel  $\kappa$  to specify the SVGD step (5) (which is an independent choice from the kernel within the GP model). The RBF kernel’s variance is set to 1, and we select the lengthscale at each iteration of SVGD using the median rule as in Liu and Wang (2016). We run experiments with  $J = 2, 5, 10$  and 20 particles (labelled SteinGP2 through to SteinGP20).

Further experimental details are given in Appendix 12.

## 5.1 UCI Datasets

We analyse 19 UCI datasets where the target is 1-dimensional. Datasets range in size from 23 to 5875 datapoints. As highlighted in Appendix 10.1, the targets in 6 of the datasets are binary, whilst the remaining 14 datasets are continuous values. To accommodate this, we use a GP with a Bernoulli likelihood for the classification tasks, and a Gaussian likelihood for regression. For regression, inference is made of the model’s hyperparameters and for classification we also infer the latent values of the GP.

When the likelihood is Gaussian, we compare our SteinGP against a GP that is fit using maximum likelihood (ML) and another GP fit using VI (VI). For Bernoulli likelihoods, maximum likelihood estimation is not feasible so we instead use Hamiltonian Monte-Carlo (HMC) for inference along with VI. In Table 2 we report the test log-likelihoods where there was a significant difference between one, or more, of the models. A full table can be found in Table 8.

From Table 2, it can be seen in all but two of the experiments that a GP inferred using SVGD significantly outperforms comparative methods. Furthermore, Table 2 shows that increasing the number of particles for SVGD leads to larger test log-likelihood values.

For two particles, a SteinGP is almost always faster than comparative methods. The only exceptions to this are when either the maximum likelihood approach converges very quickly and the difference is then of the order of seconds, or the variational approach for non-conjugate inference.



Table 3: Relative average computational runtimes of comparative methods. Results are reported relative to a SteinGP with 2 particles i.e., a value of 2 would indicate that method was two times slower than SteinGP2.

	ML	VI	HMC
Relative wall time	1.8	1.3	5.6

Across all UCI datasets we report the average runtime of each comparative method and report timings relative to a SteinGP with 2 particles Table 3. It is clear that a SteinGP is a computationally efficient model, particularly compared to a HMC approach, and a SteinGP consistently produces optimal predictive results. A full table of computational runtimes broken out by dataset can be found in Appendix 10.3.

## 5.2 Multimodal Inference

A multimodal posterior is often the result of a misspecified model. However, posterior multimodality can also occur due to corrupted data. To see this, we use the 1-dimensional example from Neal (1997) whereby data is generated according to

$$y_i = 0.3 + 0.3x_i + 0.5 \sin(2.7x_i) + \frac{1.1}{1 + x_i^2} + \epsilon_i$$

where  $x_i \sim \mathcal{N}(0, 1)$  and  $\epsilon_i \sim \mathcal{N}(0, \sigma^2)$ . We set  $\sigma = 1$  with probability 0.05, and  $\sigma = 0.1$  otherwise, thus inflating the variance of some data points and creating outliers. We simulate 200 points from this model, with the first 100 used for the fitting of the GP and remaining 100 used for evaluation Appendix 10.4.

The data are modelled using a GP that is equipped with a squared exponential kernel  $k(x, x') = \alpha^2 \exp(-(x - x')^2 / 2\ell^2)$ . We assume the observation noise follows a zero-mean Gaussian distribution with variance  $\sigma^2$ . We therefore wish to learn the posterior distribution  $p(\boldsymbol{\theta})$  where  $\boldsymbol{\theta} = \{\alpha, \ell, \sigma\}$ .

Table 4: Predictive metrics on 100 heldout datapoints from the multimodal example in Section 5.2.

	SteinGP	HMC	VI
RMSE	<b>0.39</b>	0.43	0.44
Log posterior density	<b>-24.33</b>	-24.38	-27.31
Runtime (seconds)	24.8	50.4	<b>14.7</b>

We compare the posteriors of a SteinGP with 20 particles against posteriors sampled using HMC in Figure 1. The point estimates inferred using VI are included for a full and faithful comparison. Accurately quantifying the posterior uncertainty is not only useful for parameter interpretation, but also leads to higher quality predictive inference (see Table 4). From Table 4 it is clear that at the cost of slightly longer computational runtime than VI, a SteinGP will yield significantly better predictive inference. This can be seen through the improved root-mean-square error (RMSE) of the SteinGP when compared against a VI and HMC inferred model.

### 5.3 Fully Bayesian Sparse Gaussian Process

As a final experiment, we consider a spatiotemporal air quality dataset comprised of 550,134 datapoints. Data is recorded hourly from 237 sensors across the United Kingdom (UK). The time period of interest is February 1<sup>st</sup> to April 30<sup>th</sup> 2020; the period in which the UK entered a Covid-19 lockdown. Consequently, the spatiotemporal dynamics of air quality levels are chaotic and challenging to model as many individuals adopt lifestyle changes with huge ramifications towards their contribution to air pollution (see Figure 10.6). Historically, fully Bayesian inference with GP models would be infeasible on such datasets due to the challenging scaling of MCMC samplers. However, using the batched approach in (10) we are able to make full Bayesian inference tractable.

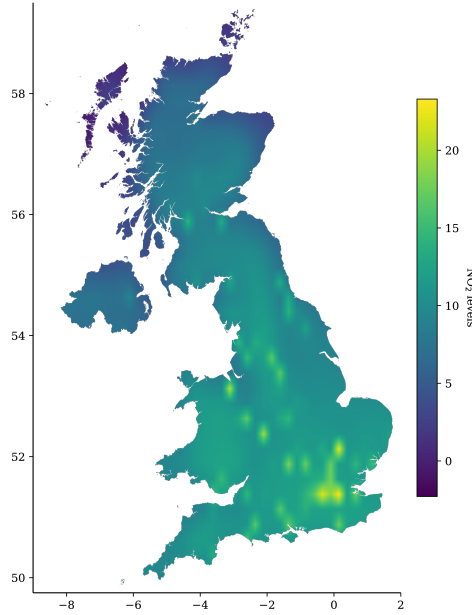


Figure 2: Inferred  $\text{NO}_2$  spatial surface ( $\mu\text{gm}^{-3}$ ) in the UK at 9AM on March 23<sup>rd</sup>; the day that initial lockdown measures were announced.

To further demonstrate the efficacy of a SteinGP, we develop, in conjunction with climate scientists, a complex separable kernel that principally captures the complex spatiotemporal dynamics of atmospheric Nitrogen Dioxide ( $\text{NO}_2$ ). Across the spatial dimensions we use a third-order Matérn kernel and in the temporal dimension we use a product of a first-order Matérn and a third-degree polynomial kernel to capture the temporal nonstationarity. We further include a white noise process. See Appendix 9 for full expressions of these kernels and Appendix 11.2 for a demo implementation of this model.

**Predictive performance** We assess the performance of our model by computing the predictive log-likelihood and the RMSE of our model and compare against the state-of-art sparse GP fitted using stochastic VI (Titsias, 2009; Hensman et al., 2013). To induce sparsity, the same set 600 inducing points are used in both models. We initialise the inducing points through a determinantal point process (DPP), as per Burt et al. (2020).

We optimise both models by running the SteinGP for 1000 iterations and the stochastic VI model for 10000. For both models, we use a batch size of 256 and a learning rate of 0.001. 30 particles are used for the SVGD routine. Due to the size of the dataset, a single step of a HMC sampler took over 10 minutes. Given that several thousand steps of the HMC sampler would be required, a comparison against HMC is infeasible.

Table 5: Comparison of our SteinGP with 30 particles against a GP fitted using stochastic VI on the air quality data of Section 5.3. Standard errors are computed by fitting each model on 5 random splits of the data, with 30% of the data being used for prediction.

	SteinGP	SVI
RMSE	$0.82 \pm 0.09$	$0.79 \pm 0.07$
Log-likelihood	$-1.358 \pm 0.15$	$-1.342 \pm 0.11$

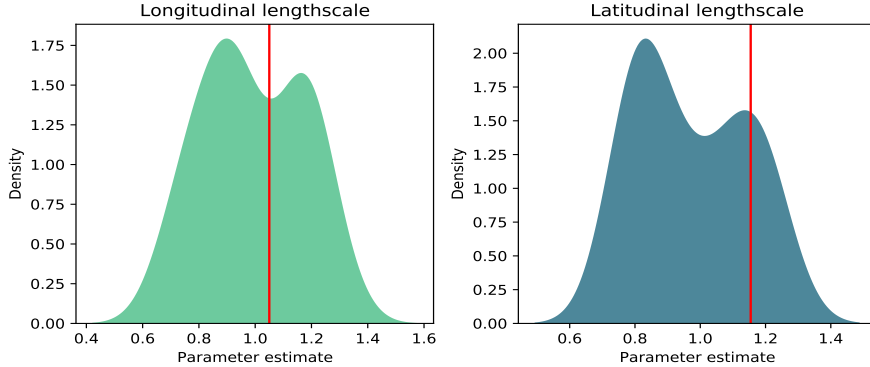


Figure 3: Spatial lengthscale posteriors for the air quality data in Section 5.3. The density for each lengthscale is estimated using the optimised particles in SVGD and the red line corresponds to the scalar estimates produced through a stochastic VI scheme.

Table 5 shows there is no significant difference between the GP fit using SVGD and stochastic VI. Unsurprisingly, VI is faster than SVGD with average computational wall times of 141 seconds and 332 seconds, respectively. However, this is to be expected due to the kernel computations that are required at each iteration of SVGD.

**Uncertainty quantification** Although the headline predictive performance of the two methods is comparable, the fully Bayesian treatment of the GP model that SVGD enables leads to full posterior inference and improved uncertainty quantification. To see this, we hold out all stations in the midlands of the UK (see the red box in Figure 4a) and re-fit both the SteinGP and the stochastic VI counterpart. We then perform spatial interpolation over the midlands of the UK from February 1<sup>st</sup> through to April 30<sup>th</sup>. In a model that is capable of generating effective predictive uncertainties, the predictive variance should be much larger over the midlands due to the lack of observations there.

Both models achieve comparable predictive metrics (Table 10). However, the purpose of this study is to assess the predictive uncertainties that each model yields. It can be seen in Figure 3 that estimating the spatial lengthscale parameters is challenging due to multimodalities. The SteinGP appears to have captured a secondary mode for each parameter. For completeness, we also give the scalar estimates produced by the stochastic VI procedure.

From Figure 4a it can be seen that the richer posterior inference provided from a SteinGP results in more reasonable posterior uncertainty estimates than those displayed in Figure 4b. This can be seen by observing the increased uncertainty over the midlands of the UK. Noting the different legend colour scaling, it can be seen in comparison that the GP inferred using stochastic VI is incapable of capturing this behaviour and yields an almost uniform predictive variance across the UK.

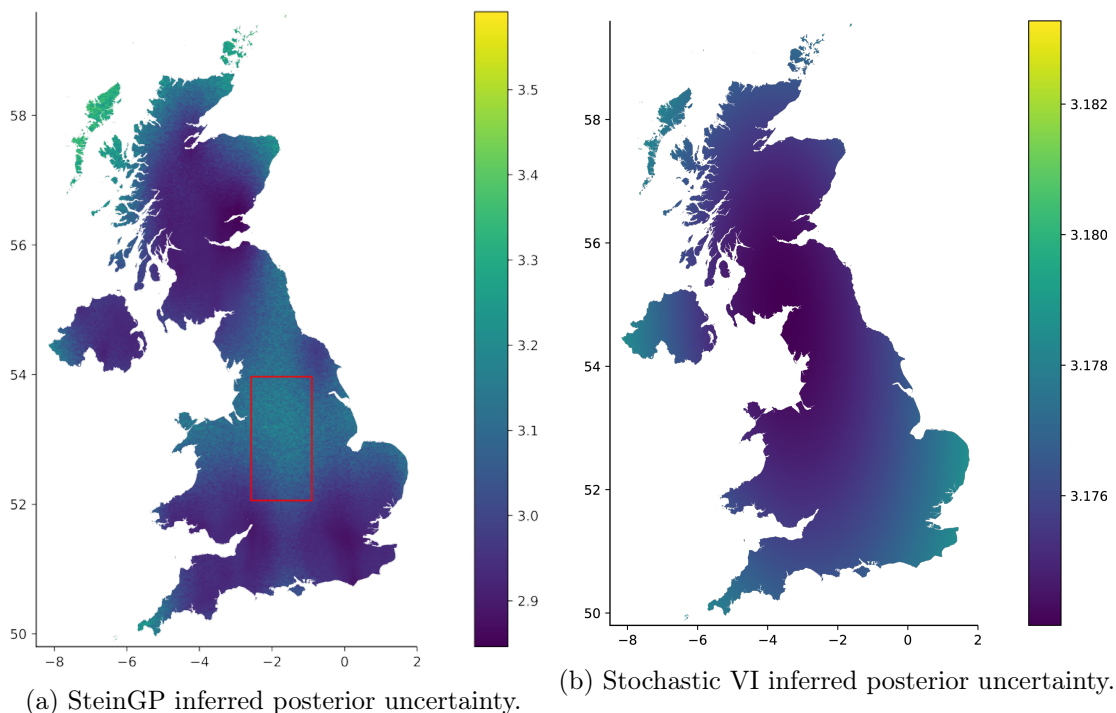


Figure 4: Posterior variances for a SteinGP (4a) and stochastic VI GP (4b). Data within the red square in 4a was held back and predictions were then made across the entire UK. The lighter colours indicate a higher predictive variance; something that is expected when there are no observation present. We note the differing colour scales used in 4a and 4b.

## 6 Discussion

We have shown that SVGD can be used to provide comparable inferential quality to the gold standard HMC sampler in GP inference, while only requiring a computational cost comparable to VI. The ability to carry out joint inference over latent function values and kernel hyperparameters allows for a full and proper consideration of uncertainty in the inference.

For simple problems where the true posterior is Gaussian, very few SVGD particles are required to achieve strong inference, as can be seen in the experiments carried out in Section 5.1. For more complex problems, such as those in Section 5.2, a large number of particles can help capture subtle posterior geometries.

Well quantified predictive uncertainties are critical when GP models are being used in real-world scenarios. As shown in Section 5.3, a SteinGP is able to provide well quantified uncertainty estimates, even in big data scenarios. This, in conjunction with strong predictive performance, makes SteinGPs a useful tool for practitioners fitting GP models.

## References

- Abadi, M., Agarwal, A., Barham, P., Brevdo, E., Chen, Z., Citro, C., Corrado, G. S., Davis, A., Dean, J., Devin, M., Ghemawat, S., Goodfellow, I., Harp, A., Irving, G., Isard, M., Jia, Y., Jozefowicz, R., Kaiser, L., Kudlur, M., Levenberg, J., Mane, D., Monga, R., Moore, S., Murray, D., Olah, C., Schuster, M., Shlens, J., Steiner, B., Sutskever, I., Talwar, K., Tucker, P., Vanhoucke, V., Vasudevan, V., Viegas, F., Vinyals, O., Warden, P., Wattenberg, M., Wicke, M., Yu, Y., and Zheng, X. (2016). TensorFlow: Large-Scale Machine Learning on Heterogeneous Distributed Systems. *arXiv:1603.04467 [cs]*. arXiv: 1603.04467.
- Berlinet, A. and Thomas-Agnan, C. (2004). *Reproducing kernel Hilbert spaces in probability and statistics*. Kluwer Academic, Boston.
- Burt, D. R., Rasmussen, C. E., and van der Wilk, M. (2020). Convergence of Sparse Variational Inference in Gaussian Processes Regression. *arXiv:2008.00323 [cs, stat]*. arXiv: 2008.00323.
- Carslaw, D. C. and Ropkins, K. (2012). openair — An R package for air quality data analysis. *Environmental Modelling & Software*, 27-28:52–61.
- Cheng, C. and Boots, B. (2017). Variational inference for gaussian process models with linear complexity. In Guyon, I., von Luxburg, U., Bengio, S., Wallach, H. M., Fergus, R., Vishwanathan, S. V. N., and Garnett, R., editors, *Advances in Neural Information Processing Systems 30: Annual Conference on Neural Information Processing Systems 2017, December 4-9, 2017, Long Beach, CA, USA*, pages 5184–5194.
- Chu, C., Minami, K., and Fukumizu, K. (2020). The equivalence between Stein variational gradient descent and black-box variational inference. In *arXiv:2004.01822 [cs, stat]*. arXiv: 2004.01822.
- Deisenroth, M. P., Fox, D., and Rasmussen, C. E. (2015). Gaussian Processes for Data-Efficient Learning in Robotics and Control. *IEEE Transactions on Pattern Analysis and Machine Intelligence*, 37(2):408–423.
- Duncan, A., Nuesken, N., and Szpruch, L. (2019). On the geometry of Stein variational gradient descent. *arXiv:1912.00894 [cs, math, stat]*. arXiv: 1912.00894.
- Gelfand, A. E., Diggle, P., Guttorp, P., and Fuentes, M. (2010). *Handbook of spatial statistics*. Chapman & Hall/CRC handbooks of modern statistical methods. CRC Press, Boca Raton, Fla.
- Gong, C., Peng, J., and Liu, Q. (2019). Quantile stein variational gradient descent for batch bayesian optimization. In Chaudhuri, K. and Salakhutdinov, R., editors, *Proceedings of the 36th International Conference on Machine Learning, ICML 2019, 9-15 June 2019, Long Beach, California, USA*, volume 97 of *Proceedings of Machine Learning Research*, pages 2347–2356. PMLR.
- Gorham, J. and Mackey, L. W. (2015). Measuring sample quality with stein’s method. In Cortes, C., Lawrence, N. D., Lee, D. D., Sugiyama, M., and Garnett, R., editors, *Advances in Neural Information Processing Systems 28: Annual Conference on Neural Information Processing Systems 2015, December 7-12, 2015, Montreal, Quebec, Canada*, pages 226–234.

- Grathwohl, W., Wang, K.-C., Jacobsen, J.-H., Duvenaud, D., and Zemel, R. (2020). Cutting out the Middle-Man: Training and Evaluating Energy-Based Models without Sampling. *arXiv:2002.05616 [cs, stat]*. arXiv: 2002.05616.
- Havasi, M., Hernández-Lobato, J. M., and Murillo-Fuentes, J. J. (2018). Inference in deep gaussian processes using stochastic gradient hamiltonian monte carlo. In Bengio, S., Wallach, H. M., Larochelle, H., Grauman, K., Cesa-Bianchi, N., and Garnett, R., editors, *Advances in Neural Information Processing Systems 31: Annual Conference on Neural Information Processing Systems 2018, NeurIPS 2018, December 3-8, 2018, Montréal, Canada*, pages 7517–7527.
- Hensman, J., de G. Matthews, A. G., Filippone, M., and Ghahramani, Z. (2015). MCMC for variationally sparse gaussian processes. In Cortes, C., Lawrence, N. D., Lee, D. D., Sugiyama, M., and Garnett, R., editors, *Advances in Neural Information Processing Systems 28: Annual Conference on Neural Information Processing Systems 2015, December 7-12, 2015, Montreal, Quebec, Canada*, pages 1648–1656.
- Hensman, J., Fusi, N., and Lawrence, N. D. (2013). Gaussian processes for big data. In Nicholson, A. and Smyth, P., editors, *Proceedings of the Twenty-Ninth Conference on Uncertainty in Artificial Intelligence, UAI 2013, Bellevue, WA, USA, August 11-15, 2013*. AUAI Press.
- Hernández-Lobato, D. and Hernández-Lobato, J. M. (2016). Scalable gaussian process classification via expectation propagation. In Gretton, A. and Robert, C. C., editors, *Proceedings of the 19th International Conference on Artificial Intelligence and Statistics, AISTATS 2016, Cadiz, Spain, May 9-11, 2016*, volume 51 of *JMLR Workshop and Conference Proceedings*, pages 168–176. JMLR.org.
- Kac, M. (1976). *Probability and related topics in physical sciences*. Number Volume 1. A in Lectures in applied mathematics. Am. Mathematical Soc, Providence, RI, 2. printing edition. OCLC: 223864829.
- Kanagawa, H., Jitkrittum, W., Mackey, L., Fukumizu, K., and Gretton, A. (2019). A Kernel Stein Test for Comparing Latent Variable Models. *arXiv*.
- Kingma, D. P. and Ba, J. (2015). Adam: A method for stochastic optimization. In Bengio, Y. and LeCun, Y., editors, *3rd International Conference on Learning Representations, ICLR 2015, San Diego, CA, USA, May 7-9, 2015, Conference Track Proceedings*.
- Korba, A., Salim, A., Arbel, M., Luise, G., and Gretton, A. (2020). A non-asymptotic analysis for stein variational gradient descent. In Larochelle, H., Ranzato, M., Hadsell, R., Balcan, M., and Lin, H., editors, *Advances in Neural Information Processing Systems 33: Annual Conference on Neural Information Processing Systems 2020, NeurIPS 2020, December 6-12, 2020, virtual*.
- Liu, H., Ong, Y.-S., Shen, X., and Cai, J. (2019). When Gaussian Process Meets Big Data: A Review of Scalable GPs. *arXiv:1807.01065 [cs, stat]*. arXiv: 1807.01065.
- Liu, Q. (2017). Stein variational gradient descent as gradient flow. In Guyon, I., von Luxburg, U., Bengio, S., Wallach, H. M., Fergus, R., Vishwanathan, S. V. N., and Garnett, R., editors, *Advances in Neural Information Processing Systems 30: Annual Conference on Neural Information Processing Systems 2017, December 4-9, 2017, Long Beach, CA, USA*, pages 3115–3123.

- Liu, Q., Lee, J. D., and Jordan, M. I. (2016). A Kernelized Stein Discrepancy for Goodness-of-fit Tests and Model Evaluation. *arXiv:1602.03253 [stat]*. arXiv: 1602.03253.
- Liu, Q. and Wang, D. (2016). Stein variational gradient descent: A general purpose bayesian inference algorithm. In Lee, D. D., Sugiyama, M., von Luxburg, U., Guyon, I., and Garnett, R., editors, *Advances in Neural Information Processing Systems 29: Annual Conference on Neural Information Processing Systems 2016, December 5-10, 2016, Barcelona, Spain*, pages 2370–2378.
- Matthews, A. G. d. G., Wilk, M. v. d., Nickson, T., Fujii, K., Boukouvalas, A., Le{\`o}n-Villagr{\`a}, P., Ghahramani, Z., and Hensman, J. (2017). GPflow: A Gaussian Process Library using TensorFlow. *Journal of Machine Learning Research*, 18(40):1–6.
- Minka, T. P. (2001). *A family of algorithms for approximate bayesian inference*. PhD Thesis, Massachusetts Institute of Technology, USA. AAI0803033.
- Mockus, J. (2012). *Bayesian Approach to Global Optimization: Theory and Applications*. Springer, Dordrecht. OCLC: 851374758.
- Murray, I., Adams, R., and MacKay, D. (2010). Elliptical slice sampling. In *Proceedings of the Thirteenth International Conference on Artificial Intelligence and Statistics*, pages 541–548.
- Neal, R. M. (1997). Monte Carlo Implementation of Gaussian Process Models for Bayesian Regression and Classification. *arXiv:physics/9701026*. arXiv: physics/9701026.
- Nguyen, T. V. and Bonilla, E. V. (2014). Automated variational inference for gaussian process models. In Ghahramani, Z., Welling, M., Cortes, C., Lawrence, N. D., and Weinberger, K. Q., editors, *Advances in Neural Information Processing Systems 27: Annual Conference on Neural Information Processing Systems 2014, December 8-13 2014, Montreal, Quebec, Canada*, pages 1404–1412.
- Oates, C. J., Girolami, M., and Chopin, N. (2017). Control functionals for Monte Carlo integration. *Journal of the Royal Statistical Society: Series B (Statistical Methodology)*, 79(3):695–718.
- Opper, M. and Archambeau, C. (2008). The Variational Gaussian Approximation Revisited. *Neural Computation*, 21(3):786–792.
- Palacios, M. B. and Steel, M. F. J. (2006). Non-Gaussian Bayesian Geostatistical Modeling. *Journal of the American Statistical Association*, 101(474):604–618.
- Papamakarios, G., Nalisnick, E., Rezende, D. J., Mohamed, S., and Lakshminarayanan, B. (2019). Normalizing Flows for Probabilistic Modeling and Inference. *arXiv:1912.02762 [cs, stat]*. arXiv: 1912.02762.
- Pu, Y., Gan, Z., Heno, R., Li, C., Han, S., and Carin, L. (2017). VAE learning via stein variational gradient descent. In Guyon, I., von Luxburg, U., Bengio, S., Wallach, H. M., Fergus, R., Vishwanathan, S. V. N., and Garnett, R., editors, *Advances in Neural Information Processing Systems 30: Annual Conference on Neural Information Processing Systems 2017, December 4-9, 2017, Long Beach, CA, USA*, pages 4236–4245.
- Quiñonero-Candela, J. and Rasmussen, C. E. (2005). A Unifying View of Sparse Approximate Gaussian Process Regression. *J. Mach. Learn. Res.*, 6:1939–1959.

- Rasmussen, C. E. and Williams, C. K. I. (2006). *Gaussian processes for machine learning*. MIT Press.
- Rudoy, D. and Wolfe, P. J. (2006). Monte Carlo Methods for Multi-Modal Distributions. In *2006 Fortieth Asilomar Conference on Signals, Systems and Computers*, pages 2019–2023. ISSN: 1058-6393.
- Salimbeni, H. (2019). Bayesian Benchmarks.
- Salimbeni, H. and Deisenroth, M. P. (2017). Doubly stochastic variational inference for deep gaussian processes. In Guyon, I., von Luxburg, U., Bengio, S., Wallach, H. M., Fergus, R., Vishwanathan, S. V. N., and Garnett, R., editors, *Advances in Neural Information Processing Systems 30: Annual Conference on Neural Information Processing Systems 2017, December 4-9, 2017, Long Beach, CA, USA*, pages 4588–4599.
- Snelson, E. and Ghahramani, Z. (2005). Sparse gaussian processes using pseudo-inputs. In *Advances in Neural Information Processing Systems 18 [Neural Information Processing Systems, NIPS 2005, December 5-8, 2005, Vancouver, British Columbia, Canada]*, pages 1257–1264.
- Stein, C. (1972). A bound for the error in the normal approximation to the distribution of a sum of dependent random variables. *Proceedings of the Sixth Berkeley Symposium on Mathematical Statistics and Probability, Volume 2: Probability Theory*.
- Titsias, M. (2009). Variational Learning of Inducing Variables in Sparse Gaussian Processes. In *Artificial Intelligence and Statistics*, pages 567–574.
- Williams, C. and Barber, D. (1998). Bayesian classification with Gaussian processes. *IEEE Transactions on Pattern Analysis and Machine Intelligence*, 20(12):1342–1351.
- Zhou, D.-X. (2008). Derivative reproducing properties for kernel methods in learning theory. *Journal of Computational and Applied Mathematics*, 220(1):456–463.



## Supplementary Material

### 7 Particle repulsion

Reminding ourselves of the update step (5) of SVGD:

$$\hat{\phi}_{\Lambda_t}(\boldsymbol{\lambda}) = \frac{1}{J} \sum_{j=1}^J \left[ \underbrace{\kappa(\boldsymbol{\lambda}_t^j, \boldsymbol{\lambda}) \nabla_{\boldsymbol{\lambda}} \log p(\boldsymbol{\lambda}_t^j)}_{\text{Attraction}} + \underbrace{\nabla_{\boldsymbol{\lambda}} \kappa(\boldsymbol{\lambda}_t^j, \boldsymbol{\lambda})}_{\text{Repulsion}} \right],$$

we demonstrate how particles are repelled from one another. If we take  $\kappa(\cdot, \cdot)$  to be the radial basis function (a valid kernel when computing Kernel Stein Discrepancy (KSD) (Gorham and Mackey, 2015)), then we have

$$\kappa(\boldsymbol{\lambda}, \boldsymbol{\lambda}') = \exp\left(\frac{\|\boldsymbol{\lambda} - \boldsymbol{\lambda}'\|^2}{-\ell^2}\right) \quad (12)$$

whereby

$$\begin{aligned} \nabla_{\boldsymbol{\lambda}} \kappa(\boldsymbol{\lambda}, \boldsymbol{\lambda}') &= -\frac{2\boldsymbol{\lambda} - 2\boldsymbol{\lambda}'}{\ell^2} \exp\left(\frac{\|\boldsymbol{\lambda} - \boldsymbol{\lambda}'\|^2}{-\ell^2}\right) \\ &= -\frac{2(\boldsymbol{\lambda} - \boldsymbol{\lambda}')}{\ell^2} \kappa(\boldsymbol{\lambda}, \boldsymbol{\lambda}'). \end{aligned} \quad (13)$$

Should particles be densely clustered, then the resultant Gram matrix will be dense. This will lead to a larger quantity being computed upon evaluation of (13), compared to when particles are sufficiently far from one another.

### 8 Proof of Theorem 1

SVGd maps particles using  $\boldsymbol{\lambda}_{t+1} = \mathcal{T}(\boldsymbol{\lambda}_t) = \boldsymbol{\lambda}_t + \epsilon \hat{\phi}(\boldsymbol{\lambda}_t)$ . Denote the corresponding mapping of densities by  $q_{t+1} = T(q_t)$ . We have that

$$\begin{aligned} \text{KL}(q_{t+1}||p) - \text{KL}(q_t||p) &= \text{KL}(T(q_t)||p) - \text{KL}(q_t||p) \\ &= \text{KL}(q_t||T^{-1}(p)) - \text{KL}(q_t||p) \\ &= \mathbb{E}_{\boldsymbol{\lambda} \sim q_t} [\log q_t(\boldsymbol{\lambda}) - \log T^{-1}(p)(\boldsymbol{\lambda})] - \mathbb{E}_{\boldsymbol{\lambda} \sim q_t} [\log q_t(\boldsymbol{\lambda}) - \log p(\boldsymbol{\lambda})] \\ &= \mathbb{E}_{\boldsymbol{\lambda} \sim q_t} [\log p(\boldsymbol{\lambda}) - \log T^{-1}(p)(\boldsymbol{\lambda})]. \end{aligned} \quad (14)$$

Under the change of variable formula for densities, we have

$$T^{-1}(p)(\boldsymbol{\lambda}) = p(\mathcal{T}(\boldsymbol{\lambda})) \cdot |\det(\nabla_{\boldsymbol{\lambda}} \mathcal{T}(\boldsymbol{\lambda}))|$$

which allows us to rewrite (14) as

$$\mathbb{E}_{\boldsymbol{\lambda} \sim q_t} \left[ \log p(\boldsymbol{\lambda}) - \log p(\boldsymbol{\lambda} + \epsilon \hat{\phi}(\boldsymbol{\lambda})) - \log |\det(\nabla_{\boldsymbol{\lambda}} \mathcal{T}(\boldsymbol{\lambda}))| \right]. \quad (15)$$

Assuming that  $\nabla_{\boldsymbol{\lambda}} \log p(\boldsymbol{\lambda})$  is Lipschitz smooth with constant  $L$  and  $\log p(\boldsymbol{\lambda}) \in C^2$ , a second order Taylor series approximation of  $\log p(\boldsymbol{\lambda} + \epsilon \hat{\phi}(\boldsymbol{\lambda}))$  about  $\boldsymbol{\lambda}$  (assuming  $\epsilon \ll 1$ ) lets us bound the first two terms in (15) by

$$\log p(\boldsymbol{\lambda}) - \log p(\boldsymbol{\lambda} + \epsilon \hat{\phi}(\boldsymbol{\lambda})) \leq -\epsilon \nabla_{\boldsymbol{\lambda}} \log p(\boldsymbol{\lambda})^\top \hat{\phi}(\boldsymbol{\lambda}) + \frac{L\epsilon^2}{2} \hat{\phi}(\boldsymbol{\lambda})^\top \hat{\phi}(\boldsymbol{\lambda}). \quad (16)$$

Noting the definition of the Stein operator from (1), we have that  $-\epsilon \nabla_{\boldsymbol{\lambda}} \log p(\boldsymbol{\lambda})^\top \hat{\phi}(\boldsymbol{\lambda}) = \text{trace}(-\epsilon \mathcal{A}_p \hat{\phi}(\boldsymbol{\lambda}) - \epsilon \nabla_{\boldsymbol{\lambda}} \hat{\phi}(\boldsymbol{\lambda}))$ . Note also that  $\mathcal{T}(\boldsymbol{\lambda}) = \boldsymbol{\lambda} + \epsilon \hat{\phi}(\boldsymbol{\lambda})$ , and therefore  $\nabla_{\boldsymbol{\lambda}} \mathcal{T}(\boldsymbol{\lambda}) = I + \epsilon \nabla_{\boldsymbol{\lambda}} \hat{\phi}(\boldsymbol{\lambda})$ . We can lower bound the final term in (15) by first noting that by the approximate Neumann expansion of the inverse matrix  $\nabla_{\boldsymbol{\lambda}} \mathcal{T}(\boldsymbol{\lambda})^{-1}$ ,

$$\nabla_{\boldsymbol{\lambda}} \mathcal{T}(\boldsymbol{\lambda})^{-1} = (I + \epsilon \nabla_{\boldsymbol{\lambda}} \hat{\phi}(\boldsymbol{\lambda}))^{-1} \approx I - \epsilon \nabla_{\boldsymbol{\lambda}} \hat{\phi}(\boldsymbol{\lambda}) + (\epsilon \nabla_{\boldsymbol{\lambda}} \hat{\phi}(\boldsymbol{\lambda}))^2 \quad (17)$$

which holds for  $0 < \epsilon \leq \rho(\nabla_{\boldsymbol{\lambda}} \hat{\phi}(\boldsymbol{\lambda}))^{-1}$ , where  $\rho(\cdot)$  is the matrix spectral norm. We can bound the final term in (15) using the following lower bound,

$$\log |\det(\nabla_{\boldsymbol{\lambda}} \mathcal{T}(\boldsymbol{\lambda}))| \geq \sum_{i=1}^d (1 - e_i^{-1}) = \text{trace}(I - \nabla_{\boldsymbol{\lambda}} \mathcal{T}(\boldsymbol{\lambda})^{-1}) \quad (18)$$

where  $e_1, \dots, e_d$  are the eigenvalues of  $\nabla_{\boldsymbol{\lambda}} \mathcal{T}(\boldsymbol{\lambda})$ . Replacing the Neumann expansion for  $\nabla_{\boldsymbol{\lambda}} \mathcal{T}(\boldsymbol{\lambda})^{-1}$  in (18), gives the following lower bound,

$$\log |\det(\nabla_{\boldsymbol{\lambda}} \mathcal{T}(\boldsymbol{\lambda}))| \geq \epsilon \nabla_{\boldsymbol{\lambda}} \cdot \hat{\phi}(\boldsymbol{\lambda}) - \epsilon^2 \|\nabla_{\boldsymbol{\lambda}} \hat{\phi}(\boldsymbol{\lambda})\|_F^2, \quad (19)$$

where  $\|\cdot\|_F$  is the Frobenius norm.

Combining (16) and (19) gives the following upper bound for (15),

$$\mathbb{E}_{\boldsymbol{\lambda} \sim q_t} \left[ -\epsilon \nabla_{\boldsymbol{\lambda}} \log p(\boldsymbol{\lambda})^\top \hat{\phi}(\boldsymbol{\lambda}) + \frac{L\epsilon^2}{2} \hat{\phi}(\boldsymbol{\lambda})^\top \hat{\phi}(\boldsymbol{\lambda}) - \epsilon \nabla_{\boldsymbol{\lambda}} \cdot \hat{\phi}(\boldsymbol{\lambda}) + \epsilon^2 \|\nabla_{\boldsymbol{\lambda}} \hat{\phi}(\boldsymbol{\lambda})\|_F^2 \right]. \quad (20)$$

$$= \underbrace{-\epsilon \mathbb{E}_{\boldsymbol{\lambda} \sim q_t} [\mathcal{A}_p \hat{\phi}(\boldsymbol{\lambda})]}_B + \underbrace{\mathbb{E}_{\boldsymbol{\lambda} \sim q_t} \left[ \underbrace{\epsilon^2 \|\nabla_{\boldsymbol{\lambda}} \hat{\phi}(\boldsymbol{\lambda})\|_F^2}_{C1} + \underbrace{\frac{L\epsilon^2}{2} \hat{\phi}(\boldsymbol{\lambda})^\top \hat{\phi}(\boldsymbol{\lambda})}_{C2} \right]}_C. \quad (21)$$

By definition of the Stein discrepancy (2),  $B = -\epsilon \mathbb{D}(q_t, p)^2$ , and (14) becomes

$$\text{KL}(q_{t+1} \| p) - \text{KL}(q_t \| p) \leq -\epsilon \mathbb{D}(q_t, p)^2 + C. \quad (22)$$

Based on this, we must now show that  $C$  is bounded, which we can do by considering each term individually.

C2: We can bound this term using the properties of the RKHS (Berlinet and Thomas-Agnan, 2004). As  $\hat{\phi} = (\hat{\phi}_1, \dots, \hat{\phi}_d)'$  and  $\hat{\phi}_i \in \mathcal{H}_0 \implies \hat{\phi} \in \mathcal{H}^d$  then

$$\begin{aligned} \|\hat{\phi}(\boldsymbol{\lambda})\|_2^2 &= \sum_{i=1}^d \hat{\phi}_i(\boldsymbol{\lambda})^2 \\ &= \sum_{i=1}^d \left( \langle \hat{\phi}_i(\cdot), \kappa(\boldsymbol{\lambda}, \cdot) \rangle_{\mathcal{H}_0} \right)^2 \text{ which follows from the RKHS properties} \\ &\leq \sum_{i=1}^d \|\hat{\phi}_i\|_{\mathcal{H}_0}^2 \|\kappa(\boldsymbol{\lambda}, \cdot)\|_{\mathcal{H}_0}^2 \text{ by Cauchy-Schwarz} \\ &= \|\hat{\phi}\|_{\mathcal{H}^d}^2 \kappa(\boldsymbol{\lambda}, \boldsymbol{\lambda}') \\ &= \mathbb{D}(q_t, p)^2 \kappa(\boldsymbol{\lambda}, \boldsymbol{\lambda}') \text{ which follows by (3)} \end{aligned} \quad (23)$$

C1: We upper bound the matrix norm  $\epsilon \|\nabla_{\lambda} \hat{\phi}(\boldsymbol{\lambda})\|_F^2$  using the same RKHS property used in C2.

$$\begin{aligned}
\left\| \nabla_{\lambda} \hat{\phi}(\boldsymbol{\lambda}) \right\|_F^2 &= \sum_{i=1}^d \sum_{j=1}^d \left( \frac{\partial \hat{\phi}_i(\boldsymbol{\lambda})}{\partial \lambda_j} \right)^2 \quad \text{from definition above and the Frobenius norm} \\
&= \sum_{i=1}^d \sum_{j=1}^d \left( \langle \hat{\phi}_i(\cdot), \partial \kappa(\boldsymbol{\lambda}, \cdot) / \partial \lambda_j \rangle_{\mathcal{H}_0} \right)^2 \quad \text{by Theorem 1 of Zhou (2008)} \\
&\leq \sum_{i=1}^d \sum_{j=1}^d \left\| \hat{\phi}_i \right\|_{\mathcal{H}_0}^2 \left\| \partial \kappa(\boldsymbol{\lambda}, \cdot) / \partial \lambda_j \right\|_{\mathcal{H}_0}^2 \quad \text{by Cauchy-Schwarz} \\
&= \left\| \hat{\phi} \right\|_{\mathcal{H}^d}^2 \nabla_{\lambda, \lambda'} \kappa(\boldsymbol{\lambda}, \boldsymbol{\lambda}') \\
&= \mathbb{D}(q_t, p)^2 \nabla_{\lambda, \lambda'} \kappa(\boldsymbol{\lambda}, \boldsymbol{\lambda}').
\end{aligned}$$

Finally, putting terms C1 and C2 together, (22) now becomes

$$\begin{aligned}
\text{KL}(q_{t+1} \| p) - \text{KL}(q_t \| p) &\leq -\epsilon \mathbb{D}(q_t, p)^2 + \epsilon^2 \mathbb{D}(q_t, p)^2 \mathbb{E}_{\boldsymbol{\lambda} \sim q_t} [\nabla_{\lambda, \lambda'} \kappa(\boldsymbol{\lambda}, \boldsymbol{\lambda})] + \frac{\epsilon^2 L}{2} \mathbb{D}(q_t, p)^2 \mathbb{E}_{\boldsymbol{\lambda} \sim q_t} [\kappa(\boldsymbol{\lambda}, \boldsymbol{\lambda})] \\
&= -\epsilon \mathbb{D}(q_t, p)^2 (1 - \epsilon \mathbb{E}_{\boldsymbol{\lambda} \sim q_t} [L \kappa(\boldsymbol{\lambda}, \boldsymbol{\lambda}) / 2 + \nabla_{\lambda, \lambda'} \kappa(\boldsymbol{\lambda}, \boldsymbol{\lambda})]).
\end{aligned}$$

## 9 Kernel expressions

Table 6: Explicit forms of the kernels used in Section 5.3 operating on an arbitrary  $\mathbf{x} \in \mathbb{R}^d$ . For Matérn kernels, the respective order is given by  $c/2 - 2$ . For notational brevity we let  $\tau = \|\mathbf{x}, \mathbf{x}'\|_2^2$ .

Kernel	$k_{\boldsymbol{\theta}}(\mathbf{x}, \mathbf{x}')$	$\boldsymbol{\theta}$
Matérn $1/2$	$\sigma^2 \exp(-\tau/\ell)$	$\{\sigma \in \mathbb{R}, \ell \in \mathbb{R}^d\}$
Matérn $5/2$	$\sigma^2 (1 + \sqrt{5}\tau/\ell + 5/3\tau^2/\ell^2) \exp(-\sqrt{5}\tau/\ell)$	$\{\sigma \in \mathbb{R}, \ell \in \mathbb{R}^d\}$
Squared exponential	$\sigma^2 \exp(-\tau/2\ell^2)$	$\{\sigma \in \mathbb{R}, \ell \in \mathbb{R}^d\}$
Polynomial ( $d$ -order)	$(\sigma^2 \mathbf{x}^\top \mathbf{x}' + \gamma)^d$	$\{\sigma \in \mathbb{R}, \gamma \in \mathbb{R}\}$
White	$\begin{cases} \sigma & \text{if } \mathbf{x} = \mathbf{x}' \\ 0 & \text{otherwise} \end{cases}$	$\{\sigma \in \mathbb{R}\}$

## 10 Further experimental details

### 10.1 UCI datasets

Table 7: Full list of the UCI datasets used in Section 5.1.  $N$  corresponds the number of observations, whilst the dimension column quantifies the dimensionality of the inputs. For datasets with a binary target, we also report the dataset’s imbalance through the proportion of observations whereby the target is positive i.e. 1.

Dataset	N	Dimension	Positive-proportion
airfoil	1503	5	-
automp	392	7	-
blood	748	5	23.8%
boston	506	13	-
breast-cancer	286	10	29.72%
challenger	23	4	-
concrete	1030	8	-
concretelump	103	7	-
fertility	100	10	12.0%
gas	2565	128	-
hepatitis	155	20	79.35%
machine	209	7	-
mammographic	961	6	46.31%
parkinsons	5875	20	-
servo	167	4	-
skillcraft	3338	19	-
spectf	267	45	79.4%
winered	1599	11	-
winewhite	4898	11	-

## 10.2 Full UCI results

Table 8: Full set of test log-likelihood values for the datasets used in Section 5.1.

Dataset	SteinGP2	SteinGP5	SteinGP10	SteinGP20	VI	ML/HMC
Airfoil	<b>0.06 ± 0.04</b>	0.06 ± 0.04	0.05 ± 0.06	0.05 ± 0.05	0.03 ± 0.03	0.03 ± 0.03
Autompg	-0.39 ± 0.09	-0.39 ± 0.09	-0.39 ± 0.09	-0.4 ± 0.09	<b>-0.39 ± 0.07</b>	-0.39 ± 0.07
Blood	-0.6 ± 0.05	-0.6 ± 0.04	-0.6 ± 0.05	-0.61 ± 0.04	<b>-0.51 ± 0.05</b>	-0.52 ± 0.06
Boston	-0.3 ± 0.12	<b>-0.28 ± 0.11</b>	-0.3 ± 0.12	-0.3 ± 0.13	-0.31 ± 0.13	-0.31 ± 0.13
Breast Cancer	-0.08 ± 0.04	-0.08 ± 0.02	-0.08 ± 0.02	<b>-0.08 ± 0.01</b>	-0.65 ± 0.09	<b>-0.08 ± 0.04</b>
Challenger	-1.53 ± 0.45	-1.52 ± 0.43	<b>-1.46 ± 0.32</b>	-1.53 ± 0.41	-1.51 ± 0.3	-1.51 ± 0.3
Concrete	-0.25 ± 0.07	-0.25 ± 0.07	-0.25 ± 0.07	-0.25 ± 0.07	<b>-0.24 ± 0.05</b>	-0.24 ± 0.05
Concretelump	1.08 ± 0.39	1.07 ± 0.41	<b>1.06 ± 0.4</b>	1.08 ± 0.39	0.13 ± 1.14	0.13 ± 1.14
Fertility	-0.44 ± 0.03	-0.44 ± 0.03	-0.43 ± 0.02	<b>-0.42 ± 0.02</b>	-0.70 ± 0.08	-0.54 ± 0.02
Gas	0.88 ± 0.11	0.88 ± 0.11	<b>0.89 ± 0.1</b>	0.88 ± 0.11	0.79 ± 0.11	0.79 ± 0.11
Hepatitis	-0.41 ± 0.07	-0.41 ± 0.07	-0.42 ± 0.07	<b>-0.4 ± 0.07</b>	-0.69 ± 0	-0.44 ± 0.04
Machine	<b>-0.51 ± 0.09</b>	-0.52 ± 0.08	-0.52 ± 0.08	-0.52 ± 0.08	-0.52 ± 0.07	-0.52 ± 0.07
Mammographic	-0.37 ± 0.03	-0.37 ± 0.03	-0.37 ± 0.03	-0.37 ± 0.03	-0.39 ± 0.03	-0.38 ± 0.04
Parkinsons	4.12 ± 0.05	4.12 ± 0.05	<b>4.14 ± 0.03</b>	4.13 ± 0.06	3.95 ± 0.04	3.95 ± 0.04
Servo	-0.48 ± 0.04	-0.43 ± 0.05	-0.41 ± 0.11	-0.41 ± 0.21	-0.39 ± 0.1	<b>-0.39 ± 0.1</b>
Skillcraft	<b>-0.99 ± 0.02</b>	-0.99 ± 0.02	-0.99 ± 0.02	-0.99 ± 0.02	-1.01 ± 0.02	-1.01 ± 0.02
Spectf	-0.26 ± 0.01	-0.26 ± 0.01	-0.26 ± 0.01	<b>-0.26 ± 0.01</b>	-0.69 ± 0	-0.68 ± 0.03
Winered	-1.17 ± 0.03	-1.17 ± 0.03	-1.17 ± 0.03	-1.17 ± 0.03	<b>-1.16 ± 0.03</b>	-1.16 ± 0.03
Winewhite	0.56 ± 0.05	0.57 ± 0.05	<b>0.57 ± 0.05</b>	0.57 ± 0.05	0.49 ± 0.05	0.55 ± 0.05

## 10.3 Computational runtimes

Table 9: Computational runtimes reported in seconds for each model assessed in Section 5.1.

Dataset	SteinGP2	SteinGP5	SteinGP10	SteinGP20	VI	ML	HMC
Airfoil	39.96 ± 1.25	74.33 ± 2.51	129.81 ± 5.36	240.74 ± 2.93	61.48 ± 5.11	<b>21 ± 1.87</b>	-
Autompg	<b>10.09 ± 1.49</b>	19.91 ± 3.53	36.11 ± 10.17	63.93 ± 8.31	29.02 ± 0.46	11.97 ± 0.21	-
Blood	57.71 ± 0.26	111.41 ± 2.06	202.47 ± 2.35	381.57 ± 2.89	33.19 ± 1.42	-	171.49 ± 0.67
Boston	24.5 ± 1.7	49.22 ± 7.06	75.34 ± 7.17	151.41 ± 22.14	40.29 ± 1.81	<b>14.05 ± 0.64</b>	-
Breast cancer	12 ± 0.49	24.01 ± 1.27	38.3 ± 0.68	70.21 ± 0.9	8.82 ± 0.07	-	141.35 ± 0.71
Challenger	9.58 ± 0.31	16.40 ± 0.5	28.42 ± 0.38	52.7 ± 0.63	8.4 ± 0.03	<b>2.55 ± 0.07</b>	-
Concrete	<b>9.67 ± 1.18</b>	65.21 ± 0.97	85.99 ± 21.05	93.73 ± 29.91	39.82 ± 0.81	13.89 ± 0.33	-
Concretelump	32.37 ± 1.91	56.66 ± 5.66	95.8 ± 10.16	175.98 ± 14.09	35.92 ± 22.12	<b>12.51 ± 8.01</b>	-
Fertility	9.91 ± 0.37	18.9 ± 0.45	33.2 ± 0.62	60.82 ± 1.8	8.71 ± 0.09	-	141.6 ± 0.42
Gas	<b>52.82 ± 0.31</b>	107.62 ± 1.29	199.79 ± 2.27	384.25 ± 3.74	245.96 ± 8.47	102.32 ± 3.21	-
Hepatitis	13.4 ± 0.47	25.84 ± 0.99	44.56 ± 1.06	81.65 ± 2.06	8.78 ± 0.05	-	141.44 ± 0.63
Machine	18.23 ± 1.5	29.56 ± 2.34	50.07 ± 3.13	97.68 ± 7.14	27.98 ± 0.93	<b>9.7 ± 0.34</b>	-
Mammographic	57.69 ± 0.59	111.91 ± 1.67	206.66 ± 4.12	391.31 ± 5.97	42.78 ± 2.19	-	190.2 ± 0.75
Parkinsons	<b>201.64 ± 1.14</b>	468.34 ± 1.49	908.08 ± 2.13	1783.14 ± 4.22	2926.05 ± 3.04	675.27 ± 1.47	-
Servo	<b>6.98 ± 0.73</b>	42.76 ± 21.21	38.15 ± 23.22	61.65 ± 15.05	23.94 ± 1.52	8.21 ± 0.56	-
Skillcraft	68.63 ± 1.24	145.9 ± 0.67	273.3 ± 0.57	530.47 ± 1.92	190.17 ± 5.35	<b>53.96 ± 1.38</b>	-
Spectf	16.09 ± 0.56	30.87 ± 0.97	53.99 ± 1.49	102.61 ± 3.61	9.16 ± 0.23	-	142.41 ± 0.52
Wine	<b>15.73 ± 0.77</b>	61.99 ± 15.93	69.02 ± 7.51	100.62 ± 9.2	48.45 ± 4.25	17.46 ± 1.31	-
Winered	16.93 ± 3.07	46.44 ± 8.93	55.55 ± 8.86	95.14 ± 16.87	28.56 ± 2.52	<b>9.83 ± 0.91</b>	-
Winewhite	<b>142.04 ± 0.59</b>	320.33 ± 1.46	616.94 ± 1.08	1210.34 ± 1.65	1232.24 ± 7.84	315.16 ± 1.63	-

## 10.4 Multimodal data

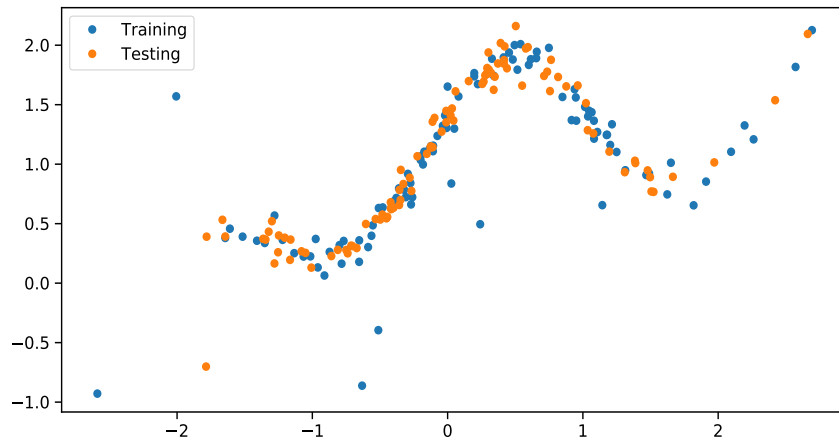


Figure 5: The multimodal dataset from Neal (1997) that is used in Section 5.2.

## 10.5 Air quality stations

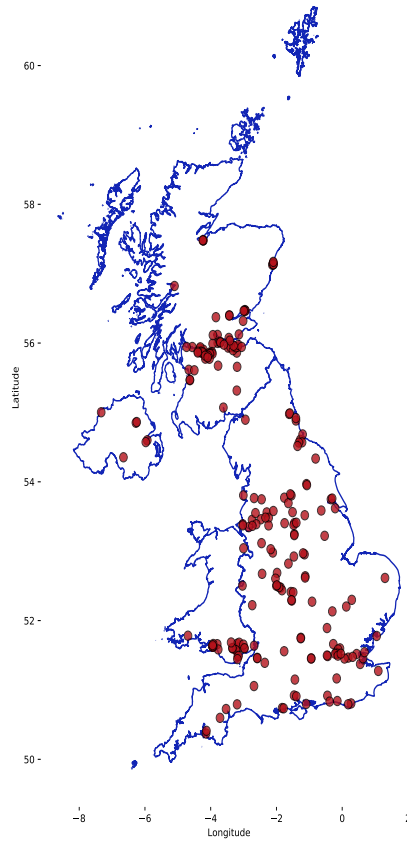


Figure 6: Spatial locations of the AURN  $\text{NO}_2$  measurement stations described in Section 5.3.

## 10.6 Temporal behaviour of air quality

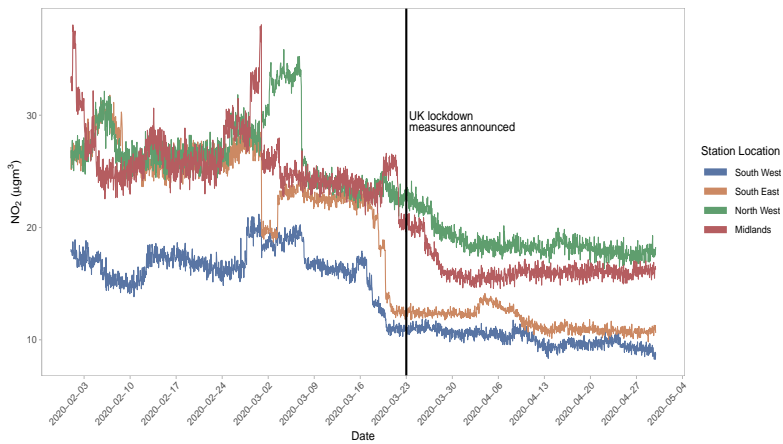


Figure 7: Example of the complex nonstationary behaviour of  $\text{NO}_2$  levels over time. Four time series originating from four stations across the UK are visualised with hourly values from February 1<sup>st</sup> through to April 30<sup>th</sup>.

## 10.7 Spatial interpolation predictive results

Table 10: Spatial interpolation of a SteinGP with 30 particles and a stochastic VI GP. Here, stations within  $(-2.2^\circ, 52^\circ)$ ,  $(-1^\circ, 54^\circ)$  are used for testing.

	SteinGP	SVI
RMSE	0.97	1.00
Log-likelihood	-1.467	-1.462

## 11 Demo implementation

### 11.1 Synthetic example

The accompanying code to this paper has been designed to integrate with GPFlow 2, and can be run through the following commands.

```
from steingp import SteinGPR, RBF, Median, SVGD
import numpy as np
import gpflow

# Build data
X = np.random.uniform(-5, 5, 100).reshape(-1,1)
y = np.sin(x)

# Define model
kernel = gpflow.kernels.SquaredExponential()
model = SteinGPR((X, y), kernel)

# Fit
opt = SVGD(model, RBF(bandwidth=Median()), n_particles=5)
opt.run(iterations = 1000)

# Predict
Xtest = np.linspace(-5, 5, 500).reshape(-1, 1)
theta = opt.get_particles()
posterior_samples = model.predict(Xtest, theta, n_samples=5)
```



## 11.2 Air quality example

```
from steingp import StochSteinGPR, RBF, Median, SVGD
import numpy as np
import pandas as pd
import tensorflow as tf
from gpflow.kernels import Matern52, Polynomial, White
from gpflow.likelihoods import Gaussian
from scipy.cluster.vq import kmeans 2

# Load data
AIR_QUALITY_DATA_PATH = ""
aq = pd.read_csv(AIR_QUALITY_DATA_PATH)
X, y = aq[:, :3].values, aq[:, 3].values

# Spatial kernel
k1 = Matern52(lengthscales=[np.sqrt(2)]*2, active_dims = [0, 1])
# Temporal kernel
k2 = Polynomial(active_dims=[2]) * Matern52(active_dims=[2])
# Gather terms
kern = k1 * k2 * White()

# Inducing points
Z = kmeans2(X, k=500, minit='points')[0]

# Define model
model = StochSteinGPR(kernel, likelihood = Gaussian(), inudcing_variables=
Z)

# Setup data
minibatch_size = 128
N = X.shape[0]
train_dataset = tf.data.Dataset.from_tensor_slices((X, y)).repeat().
shuffle(N)
train_iter = iter(train_dataset.batch(minibatch_size))

# Fit
opt = SVGD(model, train_iter, RBF(bandwidth=Median()), n_particles=30)
opt.run(iterations = 1000)

# Predict
theta = opt.get_particles()
posterior_samples = model.predict(X, theta, n_samples=5)
```

## 12 Training details

**GP kernels** For the regression and classification experiments in Section 5.1, an ARD RBF kernel was used. The same RBF kernel was used for the multimodal example in Section 5.2. A Matern32 kernel was used for the spatial inputs in in Section 5.3, whilst a third-order polynomial kernel was used for the temporal inputs. In all experiments, the kernel’s lengthscales for each dimension was initialised at the square root of the data’s dimensionality. Further, the kernel’s variance was initialised to equal 1.0.

**SVGD kernels** In all experiments we use an RBF kernel to compute (5). The kernel’s lengthscales is estimated at each iteration of the optimisation procedure using the median rule, as per Liu and Wang (2016).

**Likelihoods** For the Gaussian likelihood functions used in Section 5.1 and 5.2, the variance parameter was initialised to 1.0. The same Gaussian likelihood is used in 5.3 but no initialisation is required due to the use of priors.

**Particle initialisation** The number of particles used in the SVGD scheme is explicitly reported in the respective results. Particle initialisation is carried out by making a random draw from the respective parameter’s prior distributions where applicable, otherwise a draw is made from the uniform distribution on  $[0,1]$ .

**Prior distributions** For GP models fitted using either HMC or SVGD we place the same priors on all parameters. Unless explicitly specified, a Gamma distribution parameterised with a unit shape parameter and a scale parameter of 2 is used as the prior for all lengthscale and variance parameters.

**Parameter constraints** For all parameters where positivity is a constraint (i.e. variance), the softplus transformation is applied with a clipping of  $10^{-6}$ , as is the default in GPFlow. Optimisation is then conducted on the constrained parameter, however, we report the re-transformed parameter i.e. the unconstrained representation.

**Optimisation** For all variational models, natural gradients are used to optimise the variational parameters with a stepsize of 0.1. For the kernel hyperparameters and likelihood parameters (where applicable) in both the variational models and models fitted using maximum likelihood, the Adam optimiser (Kingma and Ba, 2015) was used. In Section 5.1 a step-size parameter of 0.05 is used, instead of the default recommendation of 0.001, as this was found to give faster optimisation at no detriment to the model’s predictive accuracy. For the multimodal and air quality experiments in section Section 5.2 and 5.3, the default Adam learning rate of 0.001 was used.

**Data availability** All datasets used in Section 5.1 are available at <https://github.com/RedactedForReview>, based upon the work in Salimbeni (2019). The multimodal data is from Neal (1997). The air quality data used in Section 5.3 was gathered using the `openaiR` package (Carslaw and Ropkins, 2012) using a script available at <https://github.com/RedactedForReview>.

**Implementation** All code for this work is written in TensorFlow (Abadi et al., 2016) and extends the popular Gaussian process library GPFlow (Matthews et al., 2017). Code to replicate experiments can be found at <https://github.com/RedactedForReview>.